Journal of Power Sources 469 (2020) 228269

Contents lists available at ScienceDirect

Journal of Power Sources

journal homepage: www.elsevier.com/locate/jpowsour

# Interface-induced degradation of amorphous carbon films/stainless steel bipolar plates in proton exchange membrane fuel cells

Hao Li [a], Peng Guo [a,**], Dong Zhang [a], Linlin Liu [a], Zhenyu Wang [a], Guanshui Ma [a], Yang Xin [a], Peiling Ke [a,b], Hidetoshi Saito [a,d], Aiying Wang [a,b,c,*]

[a] Key Laboratory of Marine Materials and Related Technologies, Zhejiang Key Laboratory of Marine Materials and Protective Technologies, Ningbo Institute of Materials Technology and Engineering, Chinese Academy of Sciences, 315201, Ningbo, PR China
[b] Center of Materials Science and Optoelectronics Engineering, University of Chinese Academy of Sciences, 100049, Beijing, PR China
[c] Ningbo Institute of Industrial Technology, Chinese Academy of Sciences, PR China
[d] Graduate School of Engineering, Nagaoka University of Technology, 940-2188, Nagaoka, Japan

## HIGHLIGHTS

- Performance of 316Lss bipolar plates in PEMFC was improved by a-C films.
- Chromium oxides were observed at the a-C/316Lss interface after corrosion test.
- Interface-induced a-C film degradation mechanism was proposed.

## GRAPHICAL ABSTRACT

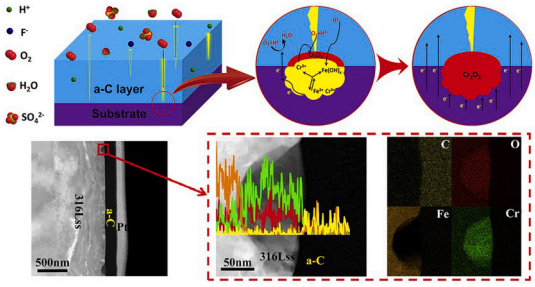


## ARTICLE INFO

*Keywords:*
Proton exchange membrane fuel cells
Metallic bipolar plates
Amorphous carbon
Contact resistance
Electrochemical corrosion
Interfacial degradation mechanism

## ABSTRACT

In the field of proton exchange membrane fuel cells (PEMFCs), amorphous carbon (a-C) films have attracted considerable attention as a surface functional coating for metallic bipolar plates (BPPs), given that they can endow metallic BPPs with both high corrosion resistance and electrical conductivity under harsh PEMFC environments. In this study, to determine the role of a-C/metallic substrate interfaces on the performance of PEMFCs, and clarify the associated degradation mechanism, a series of a-C films are deposited on 316L stainless steel (316Lss) samples at different sputtering powers. The composition, microstructure, interfacial contact resistance (ICR), and corrosion resistance of the a-C films are then systemically investigated, before and after electrochemical corrosion tests. The results obtained reveal that all the a-C films can greatly improve the performance of 316Lss under simulated PEMFC operational conditions, and the a-C film deposited at 0.9 kW exhibits the lowest corrosion current density (~$7.52 \times 10^{-3}$ μA $cm^{-2}$) and minimum ICR values (2.91 and 4.00 mΩ $cm^2$, before and after the long-time potentiostatic polarization tests, respectively). Furthermore, residual chromium oxides, which possibly result in an increased in ICR values, are observed at the a-C/316Lss interface after corrosion test; thus, an interface-induced a-C film degradation mechanism is proposed.

* Corresponding author. Key Laboratory of Marine Materials and Related Technologies, Zhejiang Key Laboratory of Marine Materials and Protective Technologies, Ningbo Institute of Materials Technology and Engineering, Chinese Academy of Sciences, 315201, Ningbo, PR China.
** Corresponding author.
*E-mail addresses:* guopeng@nimte.ac.cn (P. Guo), aywang@nimte.ac.cn (A. Wang).

https://doi.org/10.1016/j.jpowsour.2020.228269
Received 21 February 2020; Received in revised form 16 April 2020; Accepted 27 April 2020
Available online 6 June 2020

## 1. Introduction

In the past few decades, the development of proton exchange membrane fuel cells (PEMFCs) as a promising new power source for next-generation automobiles, as well as stationary and portable devices, has been rapidly increasing [1–6]. Bipolar plates (BPPs), which are a key component of PEMFCs, are required to possess an excellent electrical conductivity and a high resistance to corrosion. These properties are predominately important, given the harsh conditions under which PEMFCs are used [5–7]. Ultra-thin sheet metals, including stainless steel and titanium plates, owing to their high mechanical strength, easy formability, and low cost, are promising choices to replace traditional graphite sheets for BPPs fabrication [7–14]. Regrettably, in the combined acidic (pH = 2–5), humid, and high temperature environment in which PEMFCs are employed, loss of metallic BPPs, following the release of catalyst-poisoning ions and increased electrical resistivity, can degrade the performance of PEMFCs, especially after a long-time operation [7,15]. To overcome such drawbacks, various protective coatings, including noble metal Au/Pt films, metal carbide, and amorphous carbon (a-C) films, are being attempted, supposed that they can endow metallic BPPs with good electrical conductivity, and the same time, improve their interfacial contact resistance (ICR) as well as their corrosion resistance level [3,16,17].

Among the developed coating strategies, amorphous carbon (a-C) films are a promising material for metallic BPP protection. Their electrical conductivity and corrosive properties can be modulated by adjusting their $sp^2/sp^3$ ratio, introducing a third element, or a buff layer [18–23]. Additionally, considering the possibility of the industrial mass production and low material cost of a-C films, many studies have recently attempted to explore the performance of a-C film protected metallic BPPs, so as to clarify the associated degradation mechanism, especially with respect to long-time operation. For example, after a 7 h potentiostatic test, Wu et al. pointed out that the ICR and corrosion resistance of 316L stainless steel (316Lss) were greatly improved owing to a chromium-containing a-C film coating, and they attributed the ICR variation to a higher $sp^3/sp^2$ ratio [24]. Yi et al. conducted durability tests on a-C films for 24 h. Their investigation revealed that limited defects and the proper graphitization of a-C films could improve metallic BPP performance [25,26]. Additionally, based on molecular dynamics simulations, a more graphite-like and denser structure has been suggested for the a-C films [19]. Regarding the degradation mechanism a-C/metallic BPPs, the formation of a porous passive film [27], the increase in adsorbed oxygen content on defective sites and dangling bands on the film surface [28], and the self-passivating ability resulting from the oxidation of the metallic atoms in the a-C films [29], have been proposed. Until now, the effect of a-C films on the performance of PEMFCs has been adequately studied experimentally, and based on molecular dynamics simulations, a surface passivation degradation mechanism has been proposed. However, the role of the a-C/metallic substrate interface, which is still unclear, is usually neglected. It is possible that the corrosive electrolytes can induce certain passivation layers on the surface of uncoated metallic BPPs, and thus damaging the a-C/metallic substrate. Alternatively, the a-C/bufflayer interface could act as a key contributor to the degradation of a-C films on metallic BPPs, and then restricting the design of high-performance a-C films used in PEMFCs.

In this study, H-free a-C films were selected and deposited on 316Lss using the direct current magnetron sputter (DCMS) technique. The composition and structure of the a-C films were adjusted by changing the sputtering power, and the dependence of the $sp^2/sp^3$ ratio and $sp^2$ clusters of the a-C films on interfacial electrical conductivity and corrosion resistance was systematically investigated. In addition, no extra employed buffer-layer benefited the direct observation on evolution of a-C/316Lss interface before and after electrochemical test. After electrochemical tests in a simulated corrosive PEMFC environment, the ICR and interfacial characteristics of the a-C/316Lss system were studied to clarify the degradation mechanism, which could provide new insights regarding the designing of high-performance a-C films for metallic BPPs in PEMFCs.

## 2. Experimental details

a-C films were prepared on p-type Si (100) wafers, quartzes, and 316Lss substrates (Φ 1.5 mm × 3 mm) using the DCMS technique with a rectangular piece of graphite (dimension, 380 mm × 100 mm × 7 mm; purity, 99.99%) as the cathode target [30]. Before fixing in the chamber, all the substrates were cleaned ultrasonically using acetone and alcohol and dried using high-purity $N_2$. With the chamber vacuum bellowed at $3 \times 10^{-3}$ Pa, $Ar^+$ glow discharge was used to clean the substrates at −350 V bias for 30 min. During deposition, the negative DC bias was kept at −200 V [18,31], and a series a-C films were deposited at various target sputtering powers (0.9, 1.2, 1.5, 1.8, and 2.1 kW). By adjusting the deposition time, the thicknesses of all the a-C films was controlled to 195 ± 10 nm. Details of the deposition can be referred to our previous work [32–34].

The thickness of the deposited a-C films was measured using a surface profilometer (Alpha-Step IQ, US). The layers were deposited using a shadow mask, and the roughness and surface morphology of the a-C films were characterized using an atomic force microscope (AFM) with a scanning probe microscope tapping mode set at a scanning frequency of 2.0 Hz (3100V, Veeco, US). The Root-mean-square roughness (Rq) of the a-C films was calculated from 512 × 512 surface height data points obtained from a 1 μ m × 1 μ m scanning area. The adhesion of the a-C films to the 316Lss substrate was evaluated by a scratch test system (CSM Revetest), using a spheroconical diamond probe with an end radius of 200 μm. The scratch length was 3 mm, the maximum load was 30 N, the loading rate was 29 N/min, and the critical load value (Lc) was determined at which the catastrophic failure of the a-C film occurred. After the tests, the scratch traces were observed using optical microscopy, at least three tests were conducted for each sample.

The chemical composition of the films was characterized using X-ray photoelectron spectroscopy (XPS, Axis ultradld, Japan), while their constituent bonds were identified using monochromatic Al Kα irradiation at a pass energy of 160 eV. To preserve the original surface structure of the a-C films, no pre-treatment was employed. The $sp^2$ content and the $sp^2/sp^3$ ratio of the a-C films were determined using fitting C 1s peak. After Shirley background elimination, the mixture that fitted Gauss (20%) and Lorentz (80%) was used [35–37]. A confocal micro-Raman spectrometer (Renishaw inVia-reflex, UK, 532 nm) with a scanning range of 800–2000 $cm^{-1}$ was used to detect the carbon bond structure of the a-C films, while high-resolution transmission electron microscopy (TEM, Tecnai F20, US) was performed to observe the microstructure of the typical a-C films deposited at 0.9 kW. TEM samples were prepared using a focused ion beam (FIB) instrument (Carl Zeiss, Auriga), and Pt layer was preliminarily deposited to protect the sample surface before FIB treatment. Electron energy loss spectroscopy (EELS) measurements were conducted using a scanning-transmission electron microscopy (STEM, Tecnai F20, US). The $sp^2$ fraction was obtained by determining the area ratio of the π* and σ* states of the unknown sample and referenced to the standard highly oriented pyrolytic graphite (HOPG, 100% $sp^2$-C bonds).

Hall-effect measurements (Nanometrics, HP-5500C, US) were performed to determine the electrical resistivity of the a-C films deposited on quartz substrate. The ICR between the specimen and conductive carbon paper (Toray TGP-H-060) was evaluated as follows. During the ICR test, two carbon paper pieces were sandwiched between two gold-coated copper plates and the coated specimen [7,38]. The test pressure (1.5 MPa), which is typical of the actual mechanical loading condition in actual fuel cell stacks, was program-controlled using a universal electronic testing machine controlled by microcomputer (CMT5105, US) [39]. The external circuit was set at a constant current of 1 A using a constant current power supply, and a precision multimeter

was used to measure the voltage change of the whole circuit under different pressures. The resistance in the circuit was calculated using voltammetry.

Electrochemical corrosion measurements were performed on the Gamry electrochemical workstation (Reference 600+, US) using the conventional three-electrode cell. The samples, platinum electrode, and the Ag/AgCl electrode were used as the working, auxiliary, and reference electrodes, respectively. For potentiodyamic polarization tests at a 0.5 mV $s^{-1}$ sweep rate, a potential ranging between −0.2 and + 1.0 V vs. Ag/AgCl was used [40–42]. To evaluate carbon film corrosion stability in the simulated fuel cell cathode environment, the working electrode potential was kept constant at 0.6 V for 4 h, and to evaluate the corrosion stability of the a-C films in a simulated PEMFC cathode environment, the working electrode potential was kept constant at 0.6 V vs. Ag/AgCl for 12 h during the potentiostatic polarization tests. To simulate PEMFC operational conditions, all electrochemical experiments were conducted in a 0.5 M $H_2SO_4$ + 5 ppm HF solution at 80 °C, bubbled with pressured air. Before the tests, open-circuit potentials (OCPs) were measured for 30 min to ensure that the surface state was stable [18,31,42,43]. The electrochemical impedance spectroscopy (EIS) technique was used to evaluate the corrosion properties of all the coated and bare 316Lss substrates in simulated PEMFC solution. The EIS measurements were recorded at OCP in the frequency range of $10^5$ to $10^{-2}$ Hz with 10 mV sinusoidal perturbation. After the potentiostatic test, 100 mL solution was collected and analysed by inductively-coupled plasma optical emission spectroscopy (ICP-OES, SPECTRO ARCOSII, DE).

## 3. Results and discussion

### 3.1. Thickness, morphology and adhesion of the deposited a-C films

The deposition rate and thickness of the a-C films deposited at different sputtering powers are presented in Table 1. The average deposition rate increased monotonically from 2.4 to 5.1 nm $min^{-1}$ as the sputtering power increased from 0.9 to 2.1 kW. This observation could be attributed to the change in deposition rate per unit power, because the higher sputtering power or ion energy brings about a much higher sputtering yield, resulting in a higher deposition rate [44–46].

Even though the Rq of the a-C films increased from 1.0 nm at 0.9 kW to 1.8 nm at 2.1 kW with increasing power as shown in Table 1, all the a-C films were generally compact and dense, without any visible defects (the tapping-mode AFM morphologies of the a-C films are displayed in Fig. S1 of the supplementary materials). Usually, at higher sputtering powers, a higher deposition rate gives the newly deposited particles less time to combine in their low energy configurations [47,48], resulting in increased surface roughness, due to the atomic shadowing effect as well as the limited adatom mobility during deposition [49,50].

Scratch test was used to evaluate and compare the adhesion strength of the a-C films deposited on 316Lss. For all coated 316Lss, their adhesion strengths were around 12.5 ± 2 N (the optical micrographs of the typical scratch traces are provided in Fig. S2 of the supplementary materials), as shown in Table 1, which could be concluded that the change of sputtering power had little effect on the adhesion strength between a-C film and 316Lss substrate.

**Table 1**
Average deposition rate, thickness, Rq and adhesion of a-C films deposited at different powers.

| Power (kW) | Thickness (nm) | Deposition Rate (nm·$min^{-1}$) | Rq (nm) | Lc (N) |
|---|---|---|---|---|
| 0.9 | 188 | 2.4 | 1.0 | 12.2 |
| 1.2 | 204 | 2.9 | 1.1 | 14.0 |
| 1.5 | 198 | 3.6 | 1.4 | 12.5 |
| 1.8 | 198 | 4.0 | 1.6 | 12.4 |
| 2.1 | 203 | 5.1 | 1.8 | 11.4 |

### 3.2. Chemical composition and structure of deposited a-C films

Fig. 1(a) shows the XPS spectrum of the a-C films, where they all consisted mainly of C and O atoms. The presence of O atoms could be attributed to the residual oxygen in the vacuum chamber during film deposition, or to the oxygen adsorbed when the films were exposed to air [51,52]. Three C atom chemical states, namely $sp^2$, $sp^3$, and *C*–O/C═O hybridizations centred at 284.6, 285.4, and 286.6 eV, respectively, as shown in Fig. 1(b), were observed [37,51–53]. The $sp^2$ and $sp^3$ hybridized carbon contents of the a-C films was deduced by integrating the peak area displayed in Fig. 1(c). The results showed that as the sputtering power increased from 0.9 to 2.1 kW, the $sp^2$ content decreased from ~53 to 44%, indicating a substantially increased ionized fraction of C species in the plasma at a higher power and a higher deposition rate [44,46,54].

The Raman spectra of the a-C films deposited on a silicon substrate in the 800–2000 $cm^{-1}$ range are shown in Fig. 1(d). Usually, it is possible that after Gaussian fitting, the Raman spectra of typical amorphous carbon shows two peaks at 1350 $cm^{-1}$ (D peak) and 1560 $cm^{-1}$ (G peak) [55–57]. The G peak results from the $sp^2$ cluster structure, originating from the stretching vibration of the carbon ring and the *C*–C bonds in carbon chains, while the D peak only results from the disordered fine graphite $sp^2$ structure, originating from the breathing vibration of the carbon ring [53]. Information regarding the structure of the a-C films can be evaluated by considering the fitted half maximum of the G peak (G FWHM), the G peak position, and the peak area $I_D/I_G$ ratio values [58]. As shown in Fig. 1(e), an increase in sputtering power from 0.9 to 2.1 kW resulted in a visible increase in G FWHM from 170.7 to 180.2 $cm^{-1}$, indicating an increase in the structural disorder degree of the a-C matrix. Additionally, both the G peak position and the $I_D/I_G$ ratio decreased, with the G peak position changing slightly from 1554 to 1548 $cm^{-1}$, and the $I_D/I_G$ ratio obviously changing from its maximum value, ~3.53 at 0.9 kW to its minimum value, 2.86 at 2.1 kW. This demonstrated a decrease in $sp^2$ content and a reduction in the average size of $sp^2$ clusters with increasing sputtering power [57].

The TEM cross-sectional morphology, high resolution transmission electron microscopy (HRTEM) images, and the corresponding selected area electron diffraction (SAED) patterns of the typical a-C films prepared at 0.9 kW are shown in Fig. 2. Obviously, as displayed in Fig. 2(a), the thickness of the a-C film was ~200 nm, a finding that is consistent with the thickness measurements obtained using the surface profilometer. The corresponding SAED patterns shown in Fig. 2(b) only revealed a diffuse halo, indicating the amorphous structure of the sample. The representative EELS spectra (Fig. 2(c)) showed a clearly visible π* peak at ~285 eV, and the massif between 290 and 305 eV was rarely feature, which was also a typical signature of amorphous carbon materials [59]. Additionally, according to the fitting requirements of the double window method, the π* peak that centred at 285 eV was fitted with a Gaussian function, while the σ* peak was integrated within the small energy window between 290 and 305 eV. Using equation (1), the fraction of $sp^2$ bonded carbon atoms, x could be calculated.

$$\frac{(S\pi^*/S\sigma^*)_{film}}{(S\pi^*/S\sigma^*)_{standard}} = \frac{3-x}{4x}, \quad (1)$$

where Sπ* and Sσ* represent the π* and σ* peak integral areas, respectively, as marked by the grey area in Fig. 2(c) [60,61]. Highly oriented pyrolytic graphite (HOPG) was used as a reference. The calculated $sp^2$-C fractions from different points on the samples were all ~60%, an observation that is consistent with the results of XPS analysis.

### 3.3. Electrical and electrochemical corrosion properties of the deposited a-C films

The changes in the resistivity and I–V characteristics of the a-C films are shown in Fig. 3. All the films showed a linear I–V relationship,

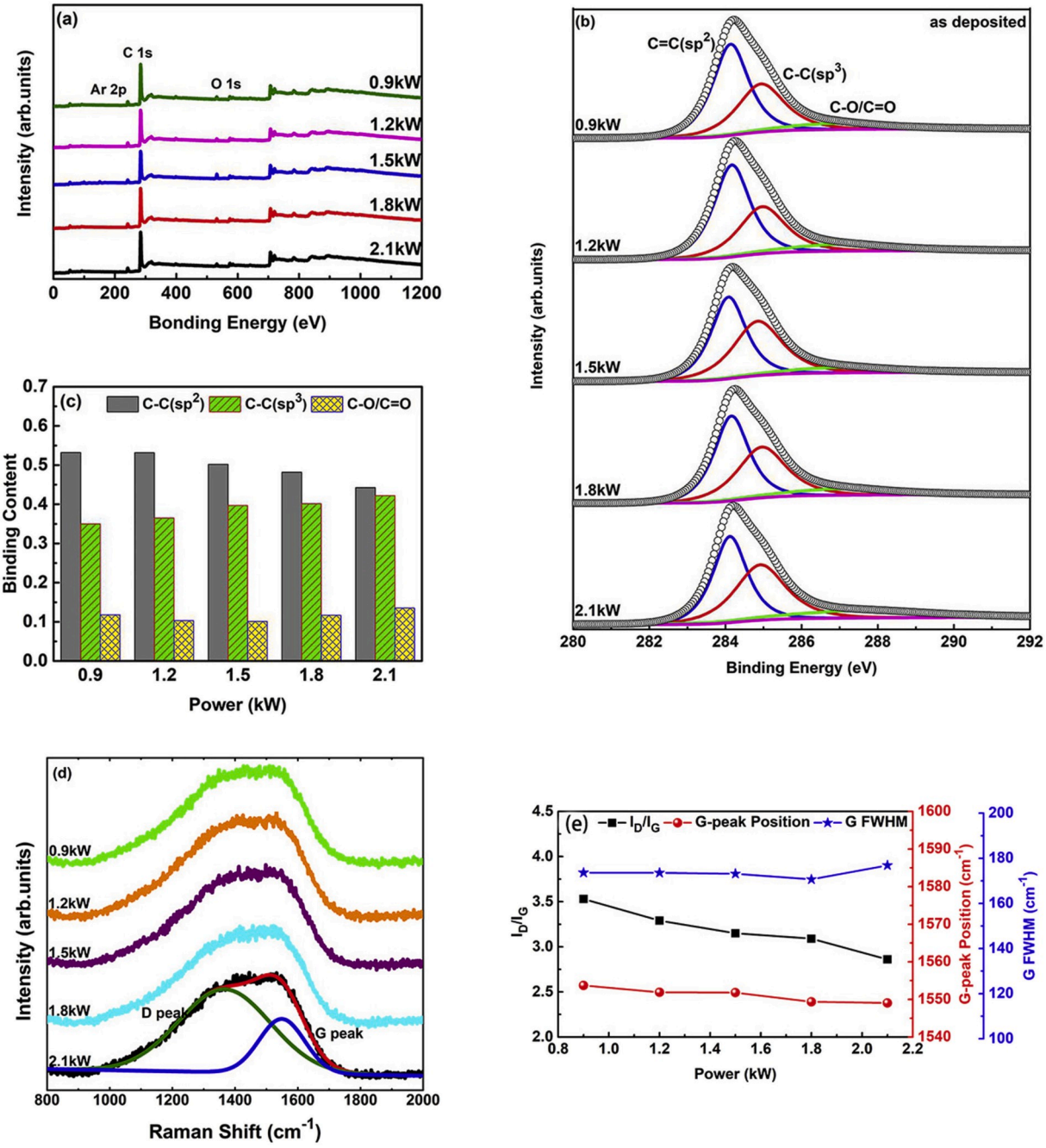


**Fig. 1.** (a) XPS spectra; (b) C 1s peaks, and (c) $sp^2$ content change of a-C films at different sputtering powers; (d) Raman spectra and (e) Corresponding fitting results of the a-C films deposited at different sputtering powers.

indicating that the carrier transport was ohmic. A plot of the resistivity (R) of the a-C films, obtained from the I–V plots against sputtering power, showed that R increased monotonically from its minimum value, $1.797 \times 10^{-3}$ Ω cm, to its maximum value, $1.027 \times 10^{-2}$ Ω cm, at 2.1 kW.

The potentiodynamic polarization curves of the a-C films between −0.2 and + 1.0 V vs. Ag/AgCl, at a 0.5 mV $s^{-1}$ sweep rate, are shown in Fig. 4(a). Apparently, compared with the bare 316Lss substrate, the coated samples showed a lower $i_{corr}$ and a higher $E_{corr}$. The self-corrosion potential of the a-C films was ~0.2 V vs. Ag/AgCl, which was ~0.3 V higher than that of bare 316Lss. Fig. 4(b) illustrates the passivation current densities observed at 0.6 V vs. Ag/AgCl, which was a typical working potential in PEMFCs. The a-C film deposited at 0.9 kW showed the best anticorrosive performance. Its corrosion current density at the applied voltage (0.6 V) was $7.52 \times 10^{-3}$ μA $cm^{-2}$, which was much lower than the 2020 technical target (1 μA $cm^{-2}$), suggested by the US Department of Energy [5,62–64]. An increase in power to 2.1 kW resulted in a rapid growth in the corresponding current densities of the a-C films to 0.113 μA $cm^{-2}$, which might be attributed to the loose structures of the a-C films induced by excess ion bombardment at a higher sputtering power.

According to the results of EIS, compared with bare 316Lss substrates, all the a-C/316Lss displayed a larger capacitive arc in Nyquist diagram, a higher low-frequency impedance and a wider phase angle platform in Bode diagram, indicating that all the a-C films greatly improved the electrochemical corrosion resistance of 316Lss in simulate

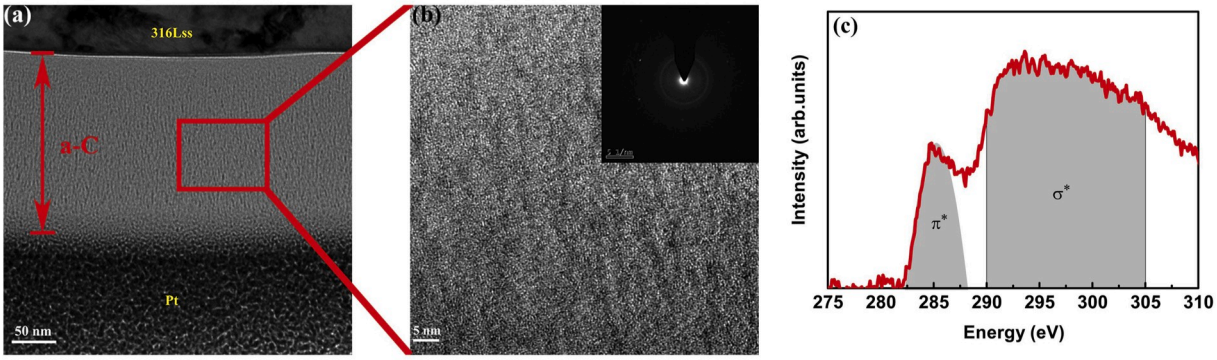


**Fig. 2.** (a) Cross-sectional TEM image, (b) HRTEM image and corresponding SAED, and (c) EELS spectra of the a-C sample deposited at 0.9 kW.

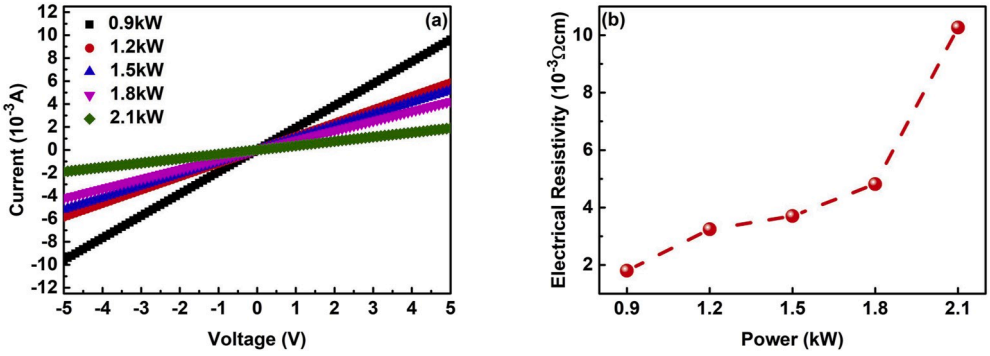


**Fig. 3.** (a) I–V characteristic plot and (b) Electrical resistivity of the a-C films deposited at different powers.

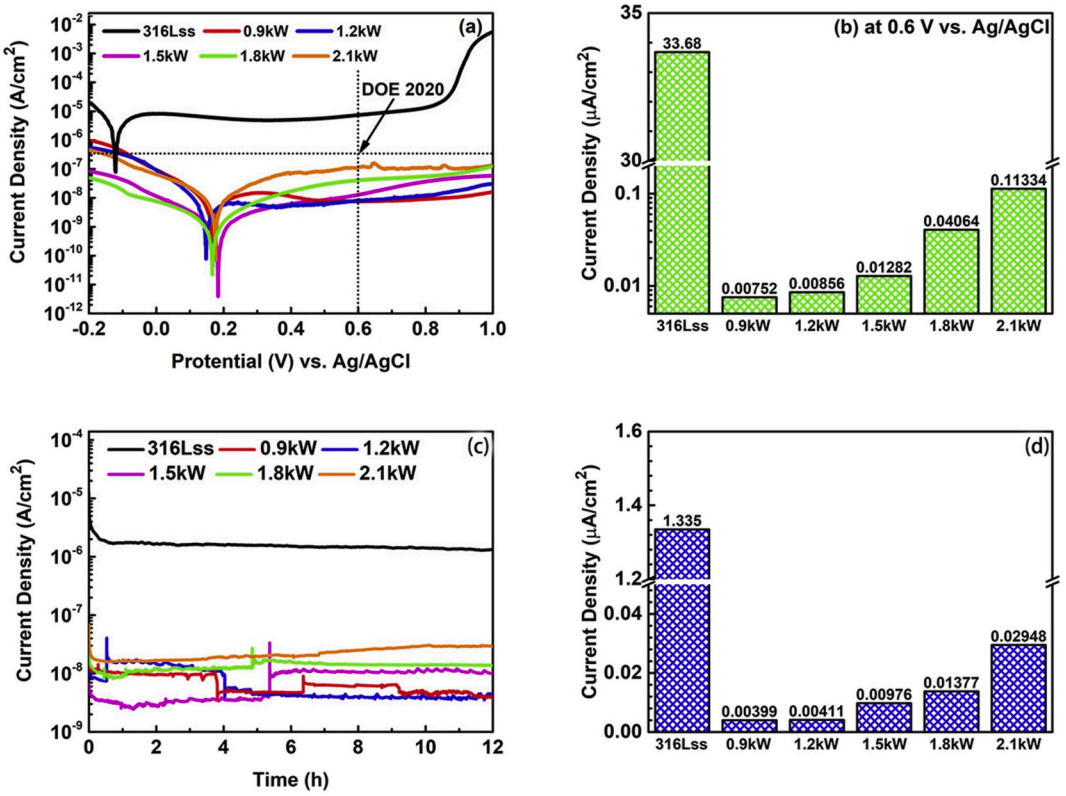


**Fig. 4.** (a) Potentiodynamic polarization curves observed between −0.2 and + 1.0 V vs. Ag/AgCl in the acid corrosion electrolyte at 80 °C; (b) Passivated current densities of all the samples at 0.6 V vs. Ag/AgCl; (c) Long-time potentiostatic tests on bare and coated 316Lss with 0.6 V vs. Ag/AgCl, in acid corrosion electrolyte at 80 °C for 12 h, and (d) Corresponding final stable current densities.

PEMFC solution (EIS result are provided in Fig. S3 of the supplementary materials). In addition, the a-C film deposited at 0.9 kW had the largest electrochemical corrosion resistance, which consisted with potentiodyamic polarization tests. Correspondingly, the polarization resistances (Rp) of the coated 316Lss substrate was at least one order of magnitude higher than that of the bare 316Lss substrate, and the a-C film deposited at 0.9 kW had the highest Rp, as shown in Table 3.

To determine the stability of the specimens, long-time (12 h) potentiostatic tests were also performed. The current density curves of the bare and coated 316Lss samples are shown in Fig. 4(c), while their final stable current densities are presented in Fig. 4(d). Compared with the bare 316Lss samples, which showed a stable current density throughout the testing period, the a-C film coated samples behaved a significant decrease in current density, which only became stable after ~5 h of testing, as shown in Fig. 4(c). In addition, an increase in power from 0.9 to 2.1 kW resulted in a gradual increase in the stable current densities of the a-C films from $3.99 \times 10^{-3}$ to a higher value, $2.948 \times 10^{-2}$ μA $cm^{-2}$, as shown in Fig. 4(d). This observation is well consistent with the potentiodynamic polarization curves of the a-C films.

The metal ions released to the solution were important parameters in gauging the properties of bipolar plate materials, because the released ions may poison the membrane electrode assembly and reduce the power output [65]. The solutions after the potentiostatic test for 12 h were collected and the dissolved Fe and Cr ions, which are the major elements in 316Lss, were determined by ICP-OES, as summarized in Table 2. For bare 316Lss, the concentrations of the Cr ions and Fe ions in the solution reached their maximum values at around 0.61 and 9.65 ppm, simultaneously, the concentration of the Fe ions was approximately 15 times larger than that of Cr ions, which implied that Fe was dissolved easily in this acidic solution [66]. With the application of a-C films, the Fe and Cr ions concentrations were remarkably reduced, which indicated that a-C films can effectively prevent 316Lss from corrosion, even no Cr signal could be detected for the samples deposited at 0.9 and 1.2 kW, suggesting that the concentration of the Cr ions was less than 0.01 ppm.

### 3.4. Electrical resistance of contact interface of the deposited a-C films

Of all the required properties of surface-modified metallic BPPs, interfacial conductivity, which can limit the high performance and life of a cell, is one of the most important properties. Thus, in this study, we focused the ICR before and after the long-time potentiostatic polarization tests, as shown in Table 3. Before the long-time potentiostatic tests, an increase in sputtering power resulted in a slight increase in the ICR value of a-C coated 316Lss samples from 2.91 to 4.00 mΩ $cm^2$. This, however, was still much lower than that of bare 316Lss samples. After the durability tests, all the samples exhibited much higher ICR values, while that of 316Lss increased by ~58.7%, i.e., from 12.10 to 19.28 mΩ $cm^2$. Furthermore, the ICR values of all the coated 316Lss increased with increasing sputtering power, and the corresponding ICR value increase ratio increased monotonously from 39.5 to 97.2%. Nevertheless, the ICR values were still at least 50% lower than those of bare 316Lss samples, indicating that the introduction of a-C films could effectively reduce the ICR, and improve 316Lss durability.

**Table 2**
Concentrations of Fe and Cr ions leached from 316Lss under simulated PEMFC operational conditions after 12 h of potentiostatic test.

| Sample | Concentrations of Fe (ppm) | Concentrations of Cr (ppm) |
|---|---|---|
| Bare 316Lss | 9.652 | 0.612 |
| a-C coated 316Lss (0.9 kW) | 0.130 | – |
| a-C coated 316Lss (1.2 kW) | 0.497 | – |
| a-C coated 316Lss (1.5 kW) | 0.864 | 0.058 |
| a-C coated 316Lss (1.8 kW) | 2.125 | 0.106 |
| a-C coated 316Lss (2.1 kW) | 3.386 | 0.306 |

**Table 3**
The Rp and ICR values of all the samples before and after the long-time potentiostatic tests.

| Sample | ICR (before tests) (mΩ·$cm^2$) | ICR (after tests) (mΩ·$cm^2$) | Rp ( $\times 10^6$ Ω $cm^2$) |
|---|---|---|---|
| Bare 316Lss | 12.10 | 19.28 | 1.01 |
| a-C coated 316Lss (0.9 kW) | 2.91 | 4.06 | 82.6 |
| a-C coated 316Lss (1.2 kW) | 3.05 | 4.78 | 72.8 |
| a-C coated 316Lss (1.5 kW) | 3.28 | 5.75 | 30.2 |
| a-C coated 316Lss (1.8 kW) | 3.54 | 6.72 | 25.4 |
| a-C coated 316Lss (2.1 kW) | 4.00 | 7.89 | 18.9 |

### 3.5. Microstructure characterization after the long-time electrochemical corrosion

Fig. 5(a) shows the C 1s core-level spectra of the samples, following the potentiostatic test that can reveal the corrosion behaviour of the a-C surface. The $sp^2/sp^3$ ratios of all the a-C films decreased to a certain degree, given that the weaker *C*-$sp^2$ bond was easily corroded in the harsh acid electrolyte compared with the stronger *C*-$sp^3$ bond [25,26,67], as shown in Fig. 5(b) and (c). Even though the *C*–O/C═O ratio remained relatively constant (Fig. 5(d)), the oxygen content of the a-C films increased by at least 250% (Fig. 5(e)), an observation that could be attributed to the corrosion of the a-C cathode environment caused by oxygen absorption [68,69].

Additionally, to evaluate the $sp^3/sp^2$ content change of the a-C films from substrate to surface, EELS was employed, and a typical sample deposited at 0.9 kW was analysed (Fig. 6). From Fig. 6(b) and (d) revealed that there was a slight change in the composition of the a-C films following the polarization test. But the $sp^3/sp^2$ content from substrate to surface remained very stable (the specific locations are labelled in Fig. 6(a) and (c)). Considering both XPS and EELS results, it was valid to conclude that after the long-time potentiostatic test, the a-C film closer to the surface was weakly oxidized, resulting in an ultra-thin $sp^3$-rich surface layer.

Further, the evolution of the interface between the 316Lss substrate and the a-C film was investigated using high-angle annular dark field (HAADF) imaging and corresponding EDS. Before the long-time potentiostatic test, a continuous and well bonded interface was clearly observed between the substrate and the a-C film, and no obvious defects existed (Fig. 7(a)). Additionally, the corresponding EDS scanning also revealed that an obvious interface existed between the substrate and a-C film (Fig. 7(b)). No oxygen-rich area was observed in the a-C films or the 316Lss substrate (Fig. 7(c)). After the long-time potentiostatic test, the morphology of the a-C film and the corresponding element distribution did not significantly change, indicating that the a-C film remained stable during electrochemical corrosion. However, in the interface, some spherical defects, ~150–200 nm were observed as shown in Fig. 7(d), and corresponding EDS scanning revealed that the defect area was rich in Cr and O elements, while Fe atoms were virtually absent, which can be explained from the dissolution of Fe, corresponding to ICP-OES test. This is because iron oxides and hydroxides cannot remain stable in such harsh acidic environments [70], while Cr atoms can remain as the anticorrosive $Cr_2O_3$ [71], which typically characterizes 316Lss in acidic environment [70–72].

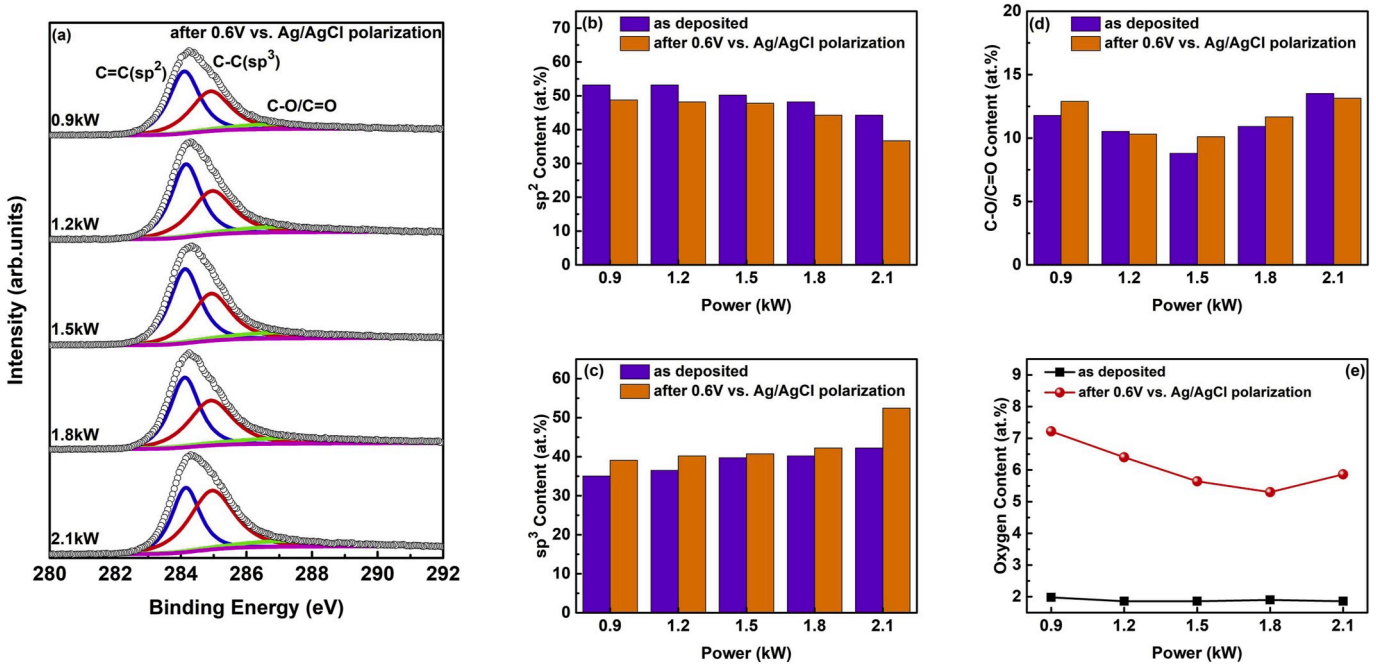


**Fig. 5.** (a) XPS spectra, (b) $sp^2$, (c) $sp^3$, (d) *C*–O/C═O, and (e) Oxygen content of the a-C films after the long-time potentiostatic test.

### 3.6. Proposed degradation mechanism

Based on the changes in the properties and microstructures of the a-C films as well as the a-C/316Lss interface before and after the potentiostatic test, two main degradation mechanisms were considered i.e., the surface oxidation of the a-C films and the interfacial corrosion between the substrate and the a-C films.

Firstly, it has been suggested in previous studies that in the harsh acid electrolytes, and under PEMFC operational conditions, the surface oxidation of a-C films may occur, and an ultra-thin $sp^3$-rich layer might be formed on the a-C film surface given that the weak *C*-$sp^2$ bond can be easily corroded [25,26,67].

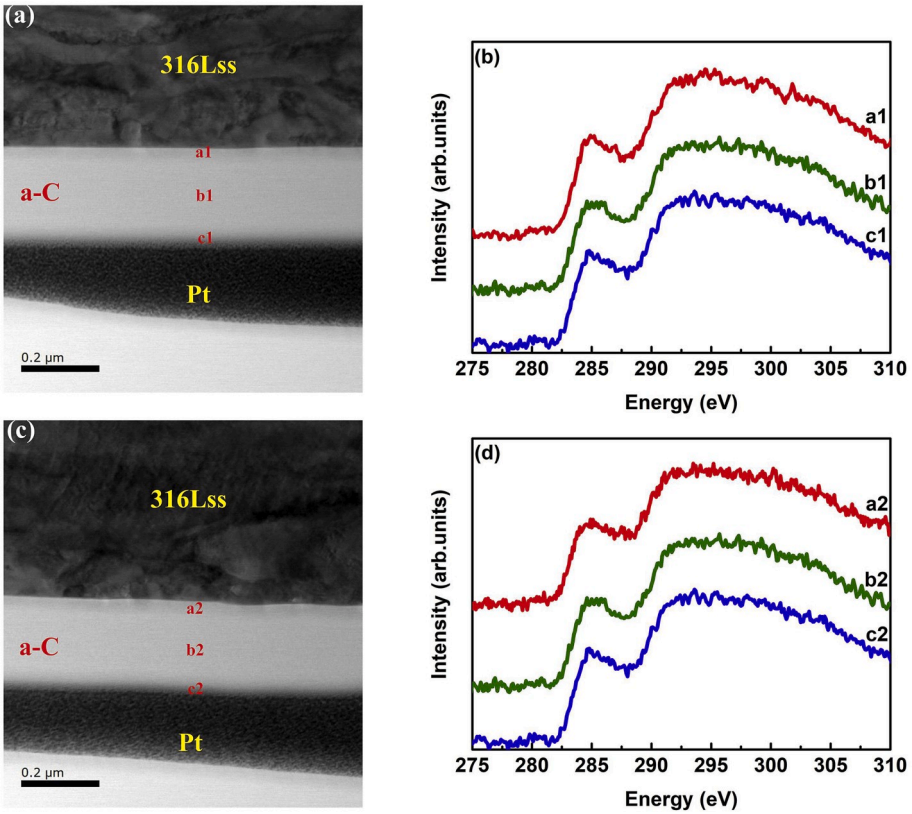


**Fig. 6.** STEM image of film deposited at 0.9 kW and EELS spectra obtained from different points on the STEM image labelled a1-c1 and a2-c2 (a, b) before and (c, d) after the long-time potentiostatic test.

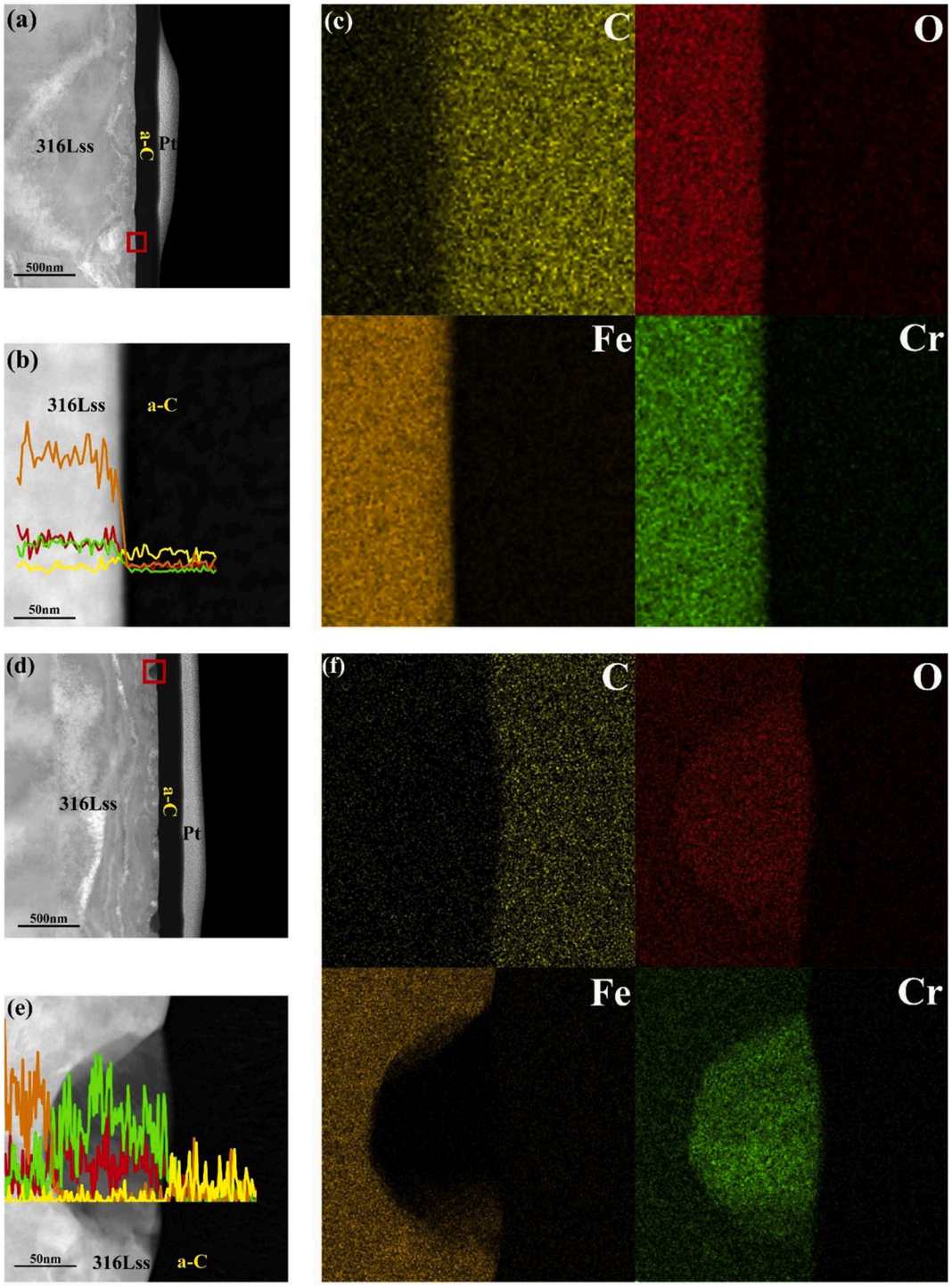


**Fig. 7.** HAADF images of the a-C films deposited at 0.9 kW, and the corresponding EDS line-scanning mapping of the red square area before (a), (b), (c) and after (d), (e), (f) the long-time potentiostatic test. (For interpretation of the references to colour in this figure legend, the reader is referred to the Web version of this article.)

Moreover, in this study, the $sp^2$ content of the as-deposited a-C films significantly decreased at elevated sputtering powers, as confirmed by the XPS and Raman spectra. The interfacial conductivities of the films also deteriorated as the number of $sp^2$-rich clusters in the a-C films decreased, a finding that is consistent with the ICR value obtained. After the long-time electrochemical corrosion test, the a-C closer to the surface was possibly oxidized slightly, forming an ultra-thin $sp^3$-rich layer in the surface, which possibly explains the uneven increase in the ICR value. However, with an increase in the sputtering power, the ICR increase ratios of the a-C films increased monotonously from 39.5 to 97.2%, an observation that is inconsistent with their $sp^2$ content, given that a-C films with higher $sp^2$ content are expected to show an inferior anticorrosive property and a larger ICR increase ratio, indicating that the a-C films/316Lss interface could also play an important role in the degradation of a-C films.

During DCMS deposition, the inevitable defects like pinholes were formed in the a-C films. Thereafter, the corrosive working liquid can reach metallic substrate through these defects in case of long-time electrochemical test, which led to the corrosion of the substrate and the subsequent porous structure. However, the stable passive layer of

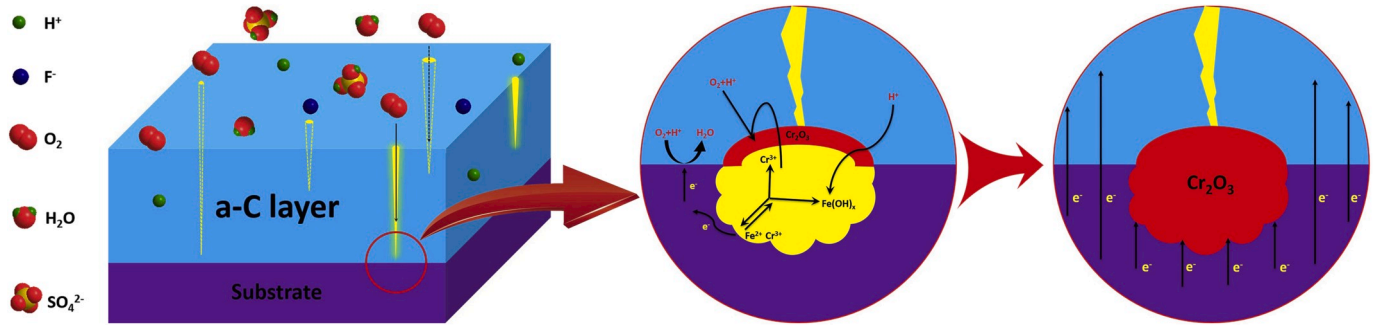


**Fig. 8.** Schematic of possible interface-induced degradation mechanism.

formed $Cr_2O_3$ on 316Lss remained in the interface, which suppressed the PEMFC carrier transport and resulted in an increase in ICR and a decreased performance. Furthermore, based on the results of the investigation of the interface between the a-C films and 316Lss, another possible interface-induced degradation mechanism of the a-C films is proposed in this study, as shown in Fig. 8.

## 4. Conclusion

In summary, a designed series of a-C films were deposited on 316Lss samples by a DCMS technique at different sputtering target powers. The influence of the a-C/316Lss substrate interface on the performance of PEMFCs was focused. All the a-C films greatly improved the performance of the metallic 316Lss BPPs under simulated PEMFC operational conditions. In particular, comparing with that observed using bare 316Lss samples, the use of the optimal a-C films (0.9 kW) could reduce the maximum corrosion current density from 33.68 to ~$7.52 \times 10^{-3}$ μA $cm^{-2}$, resulting in minimum ICR values of 2.91 and 4.00 mΩ $cm^2$ before and after the long-time potentiostatic polarization tests, respectively. Surface and interfacial analyses established that after the long-time potentiostatic tests, the morphology of the a-C films as well as their corresponding element distribution did not change remarkably. However, some Cr oxide-rich spherical defects, which could be responsible for the increased ICR, were observed in the a-C/316Lss interface. In this regard, an interface-induced a-C film degradation mechanism was also proposed for the a-C/316Lss system.

## Declaration of competing interest

The authors declare that they have no known competing financial interests or personal relationships that could have appeared to influence the work reported in this paper

## CRediT authorship contribution statement

**Hao Li:** Conceptualization, Validation, Formal analysis, Investigation, Data curation, Writing - original draft, Visualization. **Peng Guo:** Conceptualization, Investigation, Data curation, Writing - review & editing, Visualization, Project administration. **Dong Zhang:** Software, Resources, Project administration, Funding acquisition. **Linlin Liu:** Software, Investigation. **Zhenyu Wang:** Software, Investigation. **Guanshui Ma:** Investigation, Data curation, Writing - review & editing. **Yang Xin:** Investigation. **Peiling Ke:** Writing - review & editing, Project administration. **Hidetoshi Saito:** Supervision. **Aiying Wang:** Resources, Writing - review & editing, Visualization, Project administration, Funding acquisition.

## Acknowledgement

This work was financial supported by National Science and Technology Major Project (2017-VII-0012-0108), A-class pilot of the Chinese Academy of Sciences (XDA22010303), National Natural Science Foundation of China (51801226), Ningbo Science and Technology Innovation Project (2018B10014), and K.C.Wong Education Foundation (GJTD-2019-13).

## Appendix A. Supplementary data

Supplementary data to this article can be found online at https://doi.org/10.1016/j.jpowsour.2020.228269.

## References

[1] M.K. Debe, Electrocatalyst approaches and challenges for automotive fuel cells, Nature 486 (7401) (2012) 43–51.
[2] Y. Wang, K.S. Chen, J. Mishler, S.C. Cho, X.C. Adroher, A review of polymer electrolyte membrane fuel cells: Technology, applications, and needs on fundamental research, Appl. Energy 88 (4) (2011) 981–1007.
[3] B.K. Kakati, V.K. Yamsani, K.S. Dhathathreyan, D. Sathiyamoorthy, A. Verma, The electrical conductivity of a composite bipolar plate for fuel cell applications, Carbon 47 (10) (2009) 2413–2418.
[4] S.J. Lee, J.J. Lai, C.H. Huang, Stainless steel bipolar plates, J. Power Sources 145 (2) (2005) 362–368.
[5] N.F. Asri, T. Husaini, A. Sulong, E.H. Majlan, W.R.W. Daud, Coating of stainless steel and titanium bipolar plates for anticorrosion in PEMFC: a review, Int. J. Hydrogen Energy 42 (14) (2017) 9135–9148.
[6] L.F. Peng, P.Y. Yi, X.M. Lai, Design and manufacturing of stainless steel bipolar plates for proton exchange membrane fuel cells, Int. J. Hydrogen Energy 39 (36) (2014) 21127–21153.
[7] D.D. Papadias, R.K. Ahluwalia, J.K. Thomson, H.M. Meyer, M.P. Brady, H.L. Wang, et al., Degradation of SS316L bipolar plates in simulated fuel cell environment: corrosion rate, barrier film formation kinetics and contact resistance, J. Power Sources 273 (2015) 1237–1249.
[8] H.L. Wang, M.A. Sweikart, J.A. Turner, Stainless steel as bipolar plate material for polymer electrolyte membrane fuel cells, J. Power Sources 115 (2) (2003) 243–251.
[9] P.Y. Yi, D. Zhang, D.K. Qiu, L.F. Peng, X.M. Lai, Carbon-based coatings for metallic bipolar plates used in proton exchange membrane fuel cells, Int. J. Hydrogen Energy 44 (13) (2019) 6813–6843.
[10] S. Pugal Mani, N. Rajendran, Corrosion and interfacial contact resistance behavior of electrochemically nitrided 316L SS bipolar plates for proton exchange membrane fuel cells, Energy 133 (2017) 1050–1062.
[11] F.F. Bi, P.Y. Yi, T. Zhou, L.F. Peng, X.M. Lai, Effects of Al incorporation on the interfacial conductivity and corrosion resistance of CrN film on SS316L as bipolar plates for proton exchange membrane fuel cells, Int. J. Hydrogen Energy 40 (31) (2015) 9790–9802.
[12] K. Feng, Y. Shen, H.L. Sun, D.L. Liu, Q.Z. An, X. Cai, et al., Conductive amorphous carbon-coated 316L stainless steel as bipolar plates in polymer electrolyte membrane fuel cells, Int. J. Hydrogen Energy 34 (16) (2009) 6771–6777.
[13] V.V. Nikam, R.G. Reddy, Corrugated bipolar sheets as fuel distributors in PEMFC, Int. J. Hydrogen Energy 31 (13) (2006) 1863–1873.
[14] J. Wind, R. Spah, W. Kaiser, G. Bohm, Metallic bipolar plates for PEM fuel cells, J. Power Sources 105 (2) (2002) 256–260.
[15] G. Hinds, E. Brightman, Towards more representative test methods for corrosion resistance of PEMFC metallic bipolar plates, Int. J. Hydrogen Energy 40 (6) (2015) 2785–2791.
[16] P. Yi, L. Peng, T. Zhou, H. Wu, X. Lai, Development and characterization of multilayered Cr–C/a-C:Cr film on 316L stainless steel as bipolar plates for proton exchange membrane fuel cells, J. Power Sources 230 (2013) 25–31.
[17] C. Calebrese, G.A. Eisman, D.J. Lewis, L.S. Schadler, Swelling and related mechanical and physical properties of carbon nanofiber filled mesophase pitch for use as a bipolar plate material, Carbon 48 (13) (2010) 3939–3946.

[18] W. Mingge, L. Congda, H. Tao, C. Guohai, W. Donghui, Z. Haifeng, et al., Chromium interlayer amorphous carbon film for 304 stainless steel bipolar plate of proton exchange membrane fuel cell, Surf. Coating. Technol. 307 (2016) 374–381.
[19] D. Zhang, P. Yi, L. Peng, X. Lai, J. Pu, Amorphous carbon films doped with silver and chromium to achieve ultra-low interfacial electrical resistance and long-term durability in the application of proton exchange membrane fuel cells, Carbon 145 (2019) 333–344.
[20] P. Yi, D. Zhang, D. Qiu, L. Peng, X. Lai, Carbon-based coatings for metallic bipolar plates used in proton exchange membrane fuel cells, Int. J. Hydrogen Energy 44 (13) (2019) 6813–6843.
[21] K. Feng, X. Cai, H. Sun, Z. Li, P.K. Chu, Carbon coated stainless steel bipolar plates in polymer electrolyte membrane fuel cells, Diamond Relat. Mater. 19 (11) (2010) 1354–1361.
[22] H.-C. Wang, H.-H. Sheu, C.-E. Lu, K.-H. Hou, M.-D. Ger, Preparation of corrosion-resistant and conductive trivalent Cr–C coatings on 304 stainless steel for use as bipolar plates in proton exchange membrane fuel cells by electrodeposition, J. Power Sources 293 (2015) 475–483.
[23] C.E. Lu, N.W. Pu, K.H. Hou, C.C. Tseng, M.D. Ger, The effect of formic acid concentration on the conductivity and corrosion resistance of chromium carbide coatings electroplated with trivalent chromium, Appl. Surf. Sci. 282 (2013) 544–551.
[24] B. Wu, G.Q. Lin, Y. Fu, M. Hou, B.L. Yi, Chromium-containing carbon film on stainless steel as bipolar plates for proton exchange membrane fuel cells, Int. J. Hydrogen Energy 35 (24) (2010) 13255–13261.
[25] P. Yi, D. Zhang, L. Peng, X. Lai, Impact of film thickness on defects and the graphitization of nanothin carbon coatings used for metallic bipolar plates in proton exchange membrane fuel cells, ACS Appl. Mater. Interfaces 10 (40) (2018) 34561–34572.
[26] P. Yi, W. Zhang, F. Bi, L. Peng, X. Lai, Enhanced corrosion resistance and interfacial conductivity of TiC x/a-C nanolayered coatings via synergy of substrate bias voltage for bipolar plates applications in PEMFCs, ACS Appl. Mater. Interfaces 10 (22) (2018) 19087–19096.
[27] H. Luo, H.Z. Su, C.F. Dong, K. Xiao, X.G. Li, Influence of pH on the passivation behaviour of 904L stainless steel bipolar plates for proton exchange membrane fuel cells, J. Alloys Compd. 686 (2016) 216–226.
[28] F.F. Bi, K. Hou, P.Y. Yi, L.F. Peng, X.M. Lai, Mechanisms of growth, properties and degradation of amorphous carbon films by closed field unbalanced magnetron sputtering on stainless steel bipolar plates for PEMFCs, Appl. Surf. Sci. 422 (2017) 921–931.
[29] Z. Wang, K. Feng, Z. Li, F. Lu, J. Huang, Y. Wu, et al., Self-passivating carbon film as bipolar plate protective coating in polymer electrolyte membrane fuel cell, Int. J. Hydrogen Energy 41 (13) (2016) 5783–5792.
[30] X. Zuo, P.L. Ke, R.D. Chen, X.W. Li, M. Oden, A.Y. Wang, Discharge state transition and cathode fall thickness evolution during chromium HiPIMS discharge, Phys. Plasmas 24 (8) (2017), 083507.
[31] W. Mingge, L. Congda, T. Dapeng, H. Tao, C. Guohai, W. Donghui, Effects of metal buffer layer for amorphous carbon film of 304 stainless steel bipolar plate, Thin Solid Films 616 (2016) 507–514.
[32] H. Li, P. Guo, D. Zhang, R. Chen, X. Zuo, P. Ke, et al., Influence of deposition temperature on the structure, optical and electrical properties of a-C films by DCMS, Appl. Surf. Sci. 503 (2020) 144310.
[33] L. Li, L.L. Liu, X. Li, P. Guo, P. Ke, A. Wang, Enhanced tribocorrosion performance of Cr/GLC multilayered films for marine protective application, ACS Appl. Mater. Interfaces 10 (15) (2018) 13187–13198.
[34] X. Li, L. Li, D. Zhang, A. Wang, Ab initio study of interfacial structure transformation of amorphous carbon catalyzed by Ti, Cr, and W transition layers, ACS Appl. Mater. Interfaces 9 (47) (2017) 41115–41119.
[35] Y. Taki, O. Takai, XPS structural characterization of hydrogenated amorphous carbon thin films prepared by shielded arc ion plating, Thin Solid Films 316 (1–2) (1998) 45–50.
[36] P. Merel, M. Tabbal, M. Chaker, S. Moisa, J. Margot, Direct evaluation of the sp(3) content in diamond-like-carbon films by XPS, Appl. Surf. Sci. 136 (1–2) (1998) 105–110.
[37] J. Diaz, G. Paolicelli, S. Ferrer, F. Comin, Separation of the sp3 and sp2 components in the C1s photoemission spectra of amorphous carbon films, Phys. Rev. B Condens. Matter 54 (11) (1996) 8064–8069.
[38] Y. Fu, M. Hou, D. Liang, X.Q. Yan, Y.F. Fu, Z.G. Shao, et al., The electrical resistance of flexible graphite as flowfield plate in proton exchange membrane fuel cells, Carbon 46 (1) (2008) 19–23.
[39] H. Sun, K. Cooke, G. Eitzinger, P. Hamilton, B. Pollet, Development of PVD coatings for PEMFC metallic bipolar plates, Thin Solid Films 528 (2013) 199–204.
[40] H. Husby, O.A. Kongstein, A. Oedegaard, F. Seland, Carbon-polymer composite coatings for PEM fuel cell bipolar plates, Int. J. Hydrogen Energy 39 (2) (2014) 951–957.
[41] Y. Wang, D.O. Northwood, An investigation of the electrochemical properties of PVD TiN-coated SS410 in simulated PEM fuel cell environments, Int. J. Hydrogen Energy 32 (7) (2007) 895–902.
[42] Y. Wang, D.O. Northwood, Effects of O2 and H2 on the corrosion of SS316L metallic bipolar plate materials in simulated anode and cathode environments of PEM fuel cells, Electrochim. Acta 52 (24) (2007) 6793–6798.
[43] T. Wang, C.X. Zhang, X. Sun, Y.X. Guo, H. Guo, J. Tang, et al., Synthesis of ordered mesoporous boron-containing carbon films and their corrosion behavior in simulated proton exchange membrane fuel cells environment, J. Power Sources 212 (2012) 1–12.
[44] M.D. Tucker, R. Ganesan, D.G. McCulloch, J.G. Partridge, M. Stueber, S. Ulrich, et al., Mixed-mode high-power impulse magnetron sputter deposition of tetrahedral amorphous carbon with pulse-length control of ionization, J. Appl. Phys. 119 (15) (2016) 155303.
[45] S. An, J. In, H. Chang, Characteristics of the deposition rate per unit power on pulsed-DC magnetron sputtering source, Plasma Process. Polym. 6 (12) (2009) 855–859.
[46] A.A. Onoprienko, V.V. Artamonov, I.B. Yanchuk, Effect of magnetron discharge power on the resistivity and microstructure of carbon films, Surf. Coating. Technol. 200 (14–15) (2006) 4174–4178.
[47] B. Kim, S. Kim, Room-temperature high radio-frequency source power effects on silicon nitride films deposited by using a plasma-enhanced chemical vapor deposition, Met. Mater. Int. 14 (5) (2008) 637–641.
[48] Y.D. Zhao, Y.T. Qian, W.C. Yu, Z.Y. Chen, Surface roughness of alumina films deposited by reactive r.f. sputtering, Thin Solid Films 286 (1–2) (1996) 45–48.
[49] I. Petrov, P.B. Barna, L. Hultman, J.E. Greene, Microstructural evolution during film growth, J. Vac. Sci. Technol., A 21 (5) (2003) S117–S128.
[50] J.A. Thornton, The microstructure of sputter-deposited coatings, J. Vac. Sci. Technol. A-Vac. Surf. Films 4 (6) (1986) 3059–3065.
[51] P. Guo, X.W. Li, L.L. Sun, R.D. Chen, P.L. Ke, A.Y. Wang, Stress reduction mechanism of diamond-like carbon films incorporated with different Cu contents, Thin Solid Films 640 (2017) 45–51.
[52] S. Nakao, K. Yukimura, S. Nakano, H. Ogiso, DLC coating by HiPIMS: the influence of substrate bias voltage, IEEE Trans. Plasma Sci. 41 (8) (2013) 1819–1829.
[53] E. Mohagheghpour, M. Rajabi, R. Gholamipour, M.M. Larijani, S. Sheibani, Correlation study of structural, optical and electrical properties of amorphous carbon thin films prepared by ion beam sputtering deposition technique, Appl. Surf. Sci. 360 (2016) 52–58.
[54] A. Aijaz, K. Sarakinos, D. Lundin, N. Brenning, U. Helmersson, A strategy for increased carbon ionization in magnetron sputtering discharges, Diam. Relat. Mater. 23 (2012) 1–4.
[55] A.M. Ito, A. Takayama, S. Saito, H. Nakamura, Formation and classification of amorphous carbon by molecular dynamics simulation, Jpn. J. Appl. Phys. 52 (1) (2013) 7.
[56] H.X. Li, T. Xu, J.M. Chen, H.D. Zhou, H.W. Liu, The effect of applied dc bias voltage on the properties of a-C:H films prepared in a dual dc–rf plasma system, Appl. Surf. Sci. 227 (1–4) (2004) 364–372.
[57] A.C. Ferrari, J. Robertson, Interpretation of Raman spectra of disordered and amorphous carbon, Phys. Rev. B 61 (20) (2000) 14095–14107.
[58] P.K. Chu, L.H. Li, Characterization of amorphous and nanocrystalline carbon films, Mater. Chem. Phys. 96 (2–3) (2006) 253–277.
[59] R. Arenal, A.C.Y. Liu, Clustering of aromatic rings in near-frictionless hydrogenated amorphous carbon films probed using multiwavelength Raman spectroscopy, Appl. Phys. Lett. 91 (21) (2007) 211903.
[60] J. Xie, K. Komvopoulos, The effect of Argon ion irradiation on the thickness and structure of ultrathin amorphous carbon films, J. Appl. Phys. 119 (9) (2016), 095304.
[61] J.J. Cuomo, J.P. Doyle, J. Bruley, J.C. Liu, Sputter deposition of dense diamond-like carbon films at low temperature, Appl. Phys. Lett. 58 (5) (1991) 466–468.
[62] L. Mendizabal, A. Oedegaard, O.E. Kongstein, S. Leedre, J. Walmsley, J. Barriga, et al., TaNx coatings deposited by HPPMS on SS316L bipolar plates for polymer electrolyte membrane fuel cells: correlation between corrosion current, contact resistance and barrier oxide film formation, Int. J. Hydrogen Energy 42 (5) (2017) 3259–3270.
[63] Y. Zhao, L. Wei, P. Yi, L. Peng, Influence of Cr-C film composition on electrical and corrosion properties of 316L stainless steel as bipolar plates for PEMFCs, Int. J. Hydrogen Energy 41 (2) (2016) 1142–1150.
[64] J.R. Mawdsley, J.D. Carter, X.P. Wang, S. Niyogi, C.Q. Fan, R. Koc, et al., Composite-coated aluminum bipolar plates for PEM fuel cells, J. Power Sources 231 (2013) 106–112.
[65] R. Taherian, A review of composite and metallic bipolar plates in proton exchange membrane fuel cell: materials, fabrication, and material selection, J. Power Sources 265 (2014) 370–390.
[66] C.O.A. Olsson, D. Landolt, Passive films on stainless steels—chemistry, structure and growth, Electrochim. Acta 48 (9) (2003) 1093–1104.
[67] Z.Y. Wang, K. Feng, Z.G. Li, F.G. Lu, J. Huang, Y.X. Wu, et al., Self-passivating carbon film as bipolar plate protective coating in polymer electrolyte membrane fuel cell, Int. J. Hydrogen Energy 41 (13) (2016) 5783–5792.
[68] D. Persson, D. Thierry, N. LeBozec, T. Prosek, In situ infrared reflection spectroscopy studies of the initial atmospheric corrosion of Zn–Al–Mg coated steel, Corrosion Sci. 72 (2013) 54–63.
[69] C. Wang, F. Jiang, F. Wang, Cerium chemical conversion coating for aluminum alloy 2024-T3 and its corrosion resistance, Corrosion 60 (3) (2004) 237–243.
[70] K. Eguchi, Y. Ishiguro, H. Ota, Corrosion behavior of multi-phase stainless steel in 15% hydrochloric acid at a temperature of 80°C, Corrosion 71 (11) (2015) 1398–1405.
[71] Y. Yu, S. Shironita, K. Souma, M. Umeda, Effect of chromium content on the corrosion resistance of ferritic stainless steels in sulfuric acid solution, Heliyon 4 (11) (2018), e00958.
[72] L. Liu, Y. Li, F.H. Wang, Pitting mechanism on an austenite stainless steel nanocrystalline coating investigated by electrochemical noise and in-situ AFM analysis, Electrochim. Acta 54 (2) (2008) 768–780.